Optical Characterization of Graphene and Its Derivatives: An Experimentalist's Perspective

Dinh-Tuan Nguyen, Ya-Ping Hsieh, and Mario Hofmann

1 Introduction

Prof. Suzuki's arguably biggest contribution to scientific progress is a powerful method to assemble carbon atoms into extended and complex molecules. Despite the limited chemical variety, a large range of chemical properties, electronic structure, and reactivity were observed for thus produced molecules [1]. In addition to the myriad of applications, the ability to produce complex organic molecules has answered fundamental questions of the relation between a molecule's geometry and its properties and has advanced fields ranging from biology to chemical engineering.

The inverse problem, i.e. structure determination from a set of measured properties represents an important challenge for the metrology of produced species and the characterization of novel materials. This is especially taxing considering the richness of carbon chemistry as explored by Prof. Suzuki where that the substitution of a single atom can completely transform the properties of a molecule.

To enhance our understanding of the structure-property relation in complex organic molecules, a model system is needed. Ideally, such a model system would only contain carbon atoms and allow the easy addition of other species. The resulting

---

D.-T. Nguyen
Department of Material Science and Engineering, National Cheng Kung University,
Tainan 70101, Taiwan

Y.-P. Hsieh
Institute of Atomic and Molecular Sciences, Academia Sinica,
No. 1, Sec. 4, Roosevelt Rd., Taipei 10617, Taiwan

M. Hofmann (✉)
Department of Material Science and Engineering, National Cheng Kung University,
Tainan 70101, Taiwan

Department of Physics, National Taiwan University,
No.1 Sec.4 Roosevelt Road, Taipei 10617, Taiwan
e-mail: mario@phys.ntu.edu.tw

S. Kaneko et al. (eds.), *Carbon-related Materials in Recognition of Nobel Lectures by Prof. Akira Suzuki in ICCE*, DOI 10.1007/978-3-319-61651-3_2

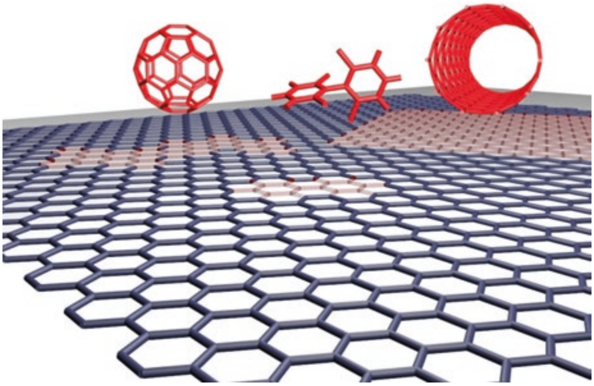

Fig. 1 Depiction of graphene and several materials that can be considered a geometric derivative of graphene

modification of characteristics would then allow inference to a heteroatom's impact on the fundamental behavior of the molecule. Furthermore, an extended molecule would be preferable to neglect effects of edges and corners. Finally, avoiding steric hindrance in the heteroatom addition implies the use of a planar structure.

Fortunately, such a model system exists in the form of graphene. The material consists of an infinite sp^2 network that contains a single atomic layer of carbon atoms. Confining the dimension of graphene in one or two directions would then lead to carbon ribbons or planar carbon molecules. The two-dimensional nature of graphene furthermore permits the formation of carbon nanotubes, fullerenes, or more complex structures by out-of-plane bending (Fig. 1). Furthermore, facile addition of heteroatoms through a large variety of functionalization methods can be achieved [2].

Thus, characterization methods that are applicable to graphene will be suitable for other forms of carbon, and trends that are observed in the modification of graphene can allow extrapolation toward unknown and complex molecules.

In this contribution, we explore the characterization of graphene and its derivatives and highlight the changes that are observed upon modifications of their geometry and chemistry. We will limit ourselves to optical characterization methods since they provide fast, nondestructive, and readily available tools to the research community.

1.1 Outline of This Chapter

This contribution is trying to set itself apart from the large amount of available literature on the topic of optical characterization of graphene by providing practical guidelines. Many times an experimentalist will try to extract specific information from a sample and needs to decide which experiments to conduct. We will here provide an overview of techniques available to elucidate certain graphene properties. Intuitive explanations are favored over details in order to facilitate understanding, and the interested reader is referred to in-depth descriptions in the form of review articles, where available.

To accommodate our result-oriented approach, this contribution is organized in the following sequence: First, a short overview of widely available optical techniques will be provided that summarizes the working principle and the requirements for sample preparation. Then, we will illustrate relevant properties of graphene and identify characterization techniques that can elucidate changes of each property.

Finally, examples of complementary experimental characterization approaches will be presented that help distinguishing competing effects.

2 Methods

2.1 Absorbance Spectroscopy

Optical absorption is among the oldest and arguably simplest characterization methods, but one that can provide important information on structure and electronic properties of materials. Also known as *UV-Vis spectroscopy*, the method in fact encompasses the spectrum in the ultraviolet, visible, and IR regions. Interaction of graphene over this wide excitation energy range is quite diverse. At low energies, the electronic response can follow the electric field, and absorption can be described by classical electrodynamics. At higher energies, graphene photon absorption causes electronic excitation akin to molecular transitions that allow inference to graphene's unique properties.

A modern double-beam UV-Vis spectrometer contains a monochromator transmitting a narrow beam of selectable wavelength from a broadband light source; an optical arrangement separating that beam into two, one of which passes through the sample while the other is used as reference; and two detectors (or one with a chopper) collecting both beams and calculating the absorbance from the intensity of the reference beam (I_0) and the signal from sample (I). Alternatively, in a single-beam setup, I_0 is acquired by running a background scan prior to sample measurement.

Absorption spectroscopy is most conveniently carried out with liquid samples, as in liquid medium the effects of diffraction, reflection, as well as bulk scattering are minimal. Solid materials can be characterized by being suspended or dissolved in solvents and placed in a transparent cuvette. Note that solvents absorb light at different degrees, which leads to a limit of operating wavelength range called cutoff wavelength (for instance, 240 nm for ethanol). Also, appropriate concentration is a crucial practical factor in obtaining a good-quality spectrum: too low concentration risks signal not being detected by the photodetector, but too high concentration may lead to saturated spectra with peaks buried in the background.

Fig. 2 Absorbance spectrum of epitaxial graphene in the infrared region and calculated results (*red curves*) [7]. *Green arrow* (*inset*) shows the absorption peak characteristic of AB-stacking bilayer graphene in the mid-IR region (Reproduced with permission from [7])

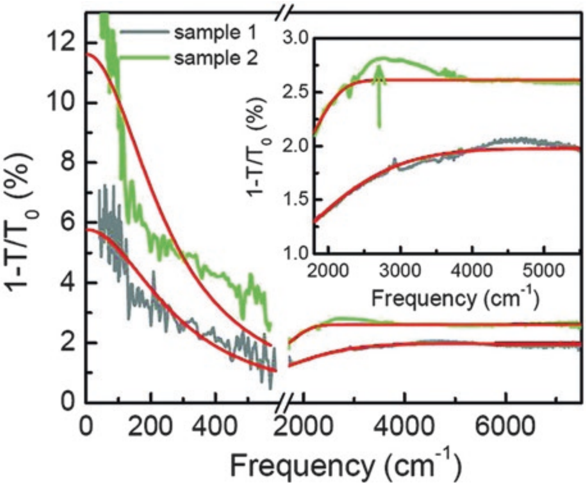

Much effort has been made to study graphene's optical conductivity in part to realize its application in optoelectronics. It was theoretically calculated [3] and later experimentally verified [4] that monolayer graphene has a constant value of absorbance of around 2.3% which is strikingly large considering its thickness. Moreover, this value is mostly independent of wavelength and solely defined by its fine structure constant and is a direct consequence of graphene's 2D nature and gapless electronic structure. Significant deviations from that universal value occur in two regions (Fig. 2). In the UV range, where a prominent peak is observed at around 4.6 eV due to an excitonic resonance [5], and the far IR range, where the scattering of free carriers dominates. For multilayer graphene, the experimental result still adheres well to predictions due to weak van der Waals interactions between layers. This, in combination with the fact that graphene reflects very little (0.1% incident light for monolayer, around 2% for ten layers), paves the way for the use of absorption measurement as a reliable method to determine the thickness and the number of layer [6].

Moreover, structural modification, either by electrostatic [8] or by chemical interactions [9], can result in band formation and band shift in absorption spectra. Absorption spectrometry therefore has been used to monitor graphene hydrogenation/dehydrogenation [10] and especially graphene oxidation/reduction. The absorption spectrum of fully oxidized graphene in visible range is dominated by a peak at around 230 nm which corresponds to $\pi \rightarrow \pi^*$ transition of C–C aromatic bonds and a less visible shoulder at about 300 nm assigned to $n \rightarrow \pi^*$ transitions of C=O bonds. From the absorption intensity, one can evaluate the level of dispersion of graphene oxide in different solvents [11]. The reduction of graphene oxide will leave a characteristic red shift (atom rearrangement) and gradual decay of these features and an overall increase in absorption intensity across the spectral range [12, 13].

2.2 Infrared Spectroscopy

Similar to optical absorption, infrared spectroscopy explores the material structure through the light absorption at certain wavelengths, in this case limited to the IR region. When investigating this region at high-frequency resolution, peaks occur in the absorbance. These are not caused by electronic transitions as described in absorbance spectroscopy but occur when there is resonance between incident radiation and molecular vibration which causes a change in dipole moment. Graphene and its derivatives are largely IR-inactive [14] due to their symmetric sp^2 bonds, but the method is sensitive to the presence of functional groups (especially oxygen) in the lattice.

Early infrared spectrometers used a dispersive element to scan sequentially over the wavelength range, which was very time-consuming and limited in resolution. This setup has been superseded in the last two decades by a much more robust Fourier transform IR (FTIR). In FTIR, a broadband light source is modulated by a Michelson interferometer with a moving mirror generating an IR excitation in the form of an interferogram. The interferogram is then deconstructed by fast Fourier transform into relevant transmittance information (hence its name).

Since the IR signal is weak, appropriate sample preparation is generally needed to ensure high-quality spectra. Because bulk absorption will result in saturated spectra, it is desirable for the sample to be made into a homogenous thin film and contained in a cell made of some IR transparent material (most often KBr, albeit NaCl, CaF_2, ZnSe, and diamond are also used). Crystalline samples are first ground into fine particles with diameters well below IR wavelengths to minimize light scattering. Then the powder is mixed with a heavy oil (Nujol) or dried KBr and pressed at high pressure into a paste or pellet. Nujol has its own absorption spectra which may interfere with a sample's spectrum, a disadvantage KBr does not have. The latter is highly hygroscopic, though, and humidity will introduce –OH group, a very strong IR absorber. One of the absorption bands of –OH lies at 1630 cm^{-1} [15] which is close to that of C=C bond, which complicates the interpretation of carbon (and organic) samples. Such difficulties can be avoided by using attenuated total reflection (ATR-FTIR) which exploits the evanescent wave near the interface of a sample with an IR sensing element upon which incident IR light is reflected. The signal only probes the sample surface, and therefore little to no sample preparation is necessary.

FTIR has been used to determine functional groups on carbon materials, such as carbon *black*, for more than three decades [17]. For graphene, as mentioned earlier, this technique is particularly sensitive in detecting oxygen-containing groups. As shown in Fig. 3, characteristic IR spectrum of graphene oxide contains absorption bands at 1720 cm^{-1} (related to C=O stretching vibrations), 1230 cm^{-1} (C–OH stretching), and 1070 cm^{-1} (C–O stretching), in addition to a band around 1620 cm^{-1} attributed to C=C stretching of the carbon lattice [18]. The reduction of graphene oxide, for example, would be manifested in FTIR by the decrease in intensity of all those bands except the C=C stretching, along with a blueshift in –OH stretching band [19]. Information obtained from FTIR can help evaluate the quality of reduced graphene oxide [16], the types, and even the orientation of various chemical groups and elements like OH, COOH [20], C–O–C [21], F [22], S [23], and H [24].

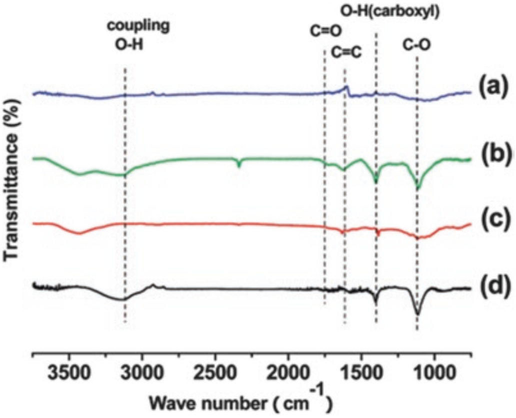

Fig. 3 FTIR transmittance spectra of pristine graphite (**a**), exfoliated graphene oxide (**b**), electrochemically reduced graphene oxide, (**c**) and chemically reduced graphene oxide (Reproduced with permission from [16])

2.3 *Raman Spectroscopy*

Raman spectroscopy is a measurement technique that analyzes the energy loss of the incident light. This approach is different from absorption techniques that characterize the loss in intensity. Energy loss occurs through interaction of incident photons with lattice vibrations or phonons in the sample. Phonons can be thought of as a harmonic oscillation of carbon atoms that exhibits a characteristic resonance frequency which depends on the coupling strength to other atoms in the crystal. While graphene and its derivatives manifest many possible vibration types, only certain "phonon modes" can couple with a photon. These "Raman-active" modes are characterized by a change in the crystal's response to an electric field upon atomic displacement around the equilibrium position.

Graphene exhibits several such Raman-active modes that are identified by their symmetry according to group theory notation (Fig. 4). A1g represents a breathing-like radial displacement of all carbon atoms within one hexagon and is termed the D-band by spectroscopists [25].

An E2g-type out-of-phase transverse displacement of neighboring carbon atoms along the zigzag direction produces phonons with a higher energy, termed optical phonon, which creates the G-band [26]. Weaker Raman features include the D'-band which originates from a similar symmetry as the G-band but exhibits a longitudinal displacement of neighboring carbon atoms [27].

Each phonon will cause reemission of the incident light with a distinct energy loss that is centered at its resonance frequency. Thus, the intensity distribution of the scattered outgoing light represents a measure of the concentration and availability of phonons and their resonance frequency. Traditionally, the unit of energy loss in such Raman spectra is in wavenumbers (cm^{-1}) which represents the reciprocal wavelength and can be related to energy loss by

$$\Delta E = \text{hc}\left(\frac{1}{\lambda_{\text{incident}}} - \frac{1}{\lambda_{\text{scattered}}}\right)$$

where h is the Planck constant and c is the speed of light.

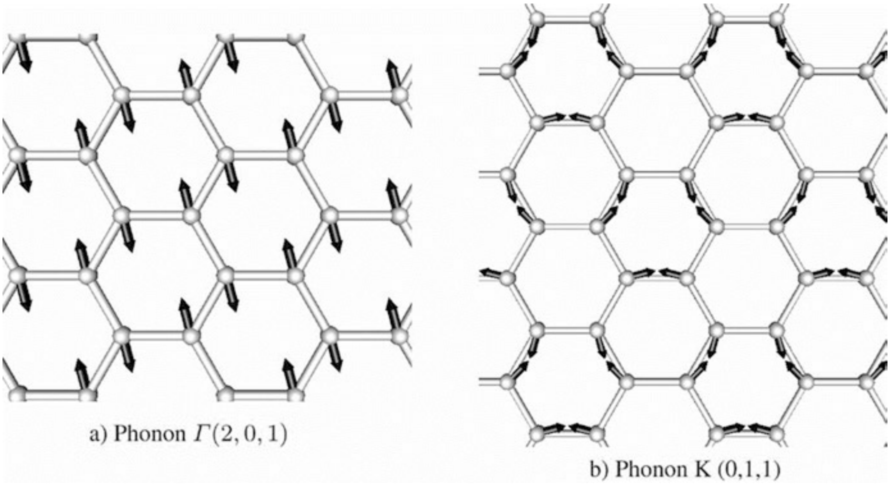

Fig. 4 Representation of symmetry of (**a**) G-band and (**b**) D-band phonon modes (Reproduced with permission from [25])

Fig. 5 Representative Raman spectra of pristine graphene (*top*) and defected graphene (*bottom*) (Reproduced with permission from [28])

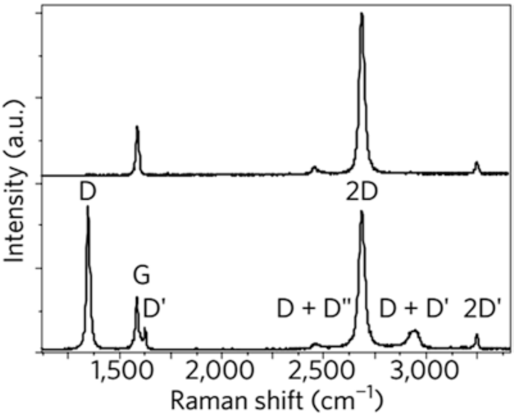

Figure 5 shows a representative Raman spectrum that exhibits distinctive energy losses to the described D-band, G-band, and G'-band phonons at 1350 cm^{-1}, 1600 cm^{-1}, and 1620 cm^{-1}, respectively. Additionally, second-order Raman features can be observed where simultaneous loss to two phonons occurs. The most prominent of these modes is the 2D-band around 2700 cm^{-1} which creates two D-band phonons.

In this description, we have only considered the creation of phonons by incident light which is termed the Stokes condition. Phonon annihilation, on the other hand, would impart additional energy to the outgoing light, and a negative value for the energy loss would occur. This "anti-Stokes condition" follows the same principle as Stokes scattering and can be treated equivalently. It has to be noted, however, that many Raman measurement systems will only allow access to the Stokes portion of the spectrum to reduce the setup's complexity.

Lasers are used as light sources due to their frequency stability and high spectral power, and several approaches exist to introduce them. For high-resolution measurements, the incident light will be tightly focused through a microscope objective whose resolution can be further enhanced through confocal illumination methods. To collect the outgoing light, a second objective can be employed in a transmission arrangement which requires transparent samples. Alternatively, the outgoing light can be collected with the same objective which, means the incident and outgoing light is sharing the same beam path. To separate them, a half-reflective mirror can be employed which reduces the intensity of the signal. If resolution is not a concern, fiber and free-space coupling in either reflection or transmission geometry can be employed which affords very compact and robust devices for mobile use. [28].

Due to the inherently weak interaction, the Raman signal is approximately 10^9 times weaker than the incident light, and high-quality filters and detectors have to be employed to overcome noise limits from sources and electronics.

Despite these challenges, Raman spectroscopy is a commonly used metrology tool due to its ability to characterize graphene in a variety of environments including in liquids and powders.

The detection efficiency can be significantly enhanced by proper sample preparation. The Raman intensity scales with the fourth power of the incident electric field, and several schemes exist to enhance it. First, improvements in Raman intensity can be achieved by tightly focusing the light. Second, suitable substrates can be employed that enhance the reflected light intensity by producing standing waves and positioning the sample at a maximum of this standing wave. Such an enhancement can be achieved in Si samples when an oxide of suitable thickness, such as 90 nm or 300 nm, is deposited. In contrast, conductive substrates will decrease the Raman intensity because they produce nodes in electrical field close to the surface. Lastly, electric field enhancement can be accomplished by producing standing waves or plasmons in the vicinity of the sample. This process is called “surface-enhanced Raman scattering” and can be introduced through suitable nanoparticles or sharp features, such as tips or gratings [29].

2.4 Rayleigh Imaging

When light interacts with the carbon lattice, most of the resulting scattering events are of elastic nature (Rayleigh scattering). Though the elastically scattered signal carries less information on a material’s structure compared to Raman scattering, its intensity is several orders higher than the latter and therefore more favorable for imaging applications.

To do this, however, one has to find ways to minimize the background effect of substrate scattering. A common setup to enhance the contrast and spatial resolution is confocal microscopy in which the scattered light from an observed spot is spatially filtered by a pinhole in the beam path, but even then the substrate’s signal can still be stronger than sample’s. This can be solved by suspending graphene to

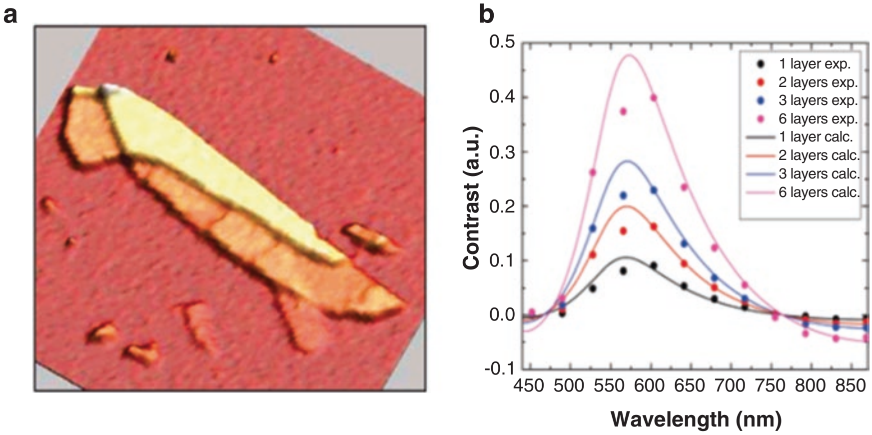

Fig. 6 A monochromatic confocal Rayleigh mapping of graphene (**a**) and contrast value as a function of number of layer (b) (Reproduced with permission from [31])

separate it from substrate, which has been realized before on carbon nanotubes, but such delicate and expensive process is often impractical [30]. Alternatively, an interferometric configuration can be employed to exploit the background signal as a reference and to increase the signal-to-noise ratio. Here the contrast is defined as $\delta = (I_{\mathrm{Si}} - I)/I_{\mathrm{Si}}$ and depends on the thickness and refractive index of the oxide layer playing the role of a spacer between Si substrate and graphene. The light source can be monochromatic like in the case of Raman spectroscopy or broadband, thanks to the recent availability of supercontinuum light sources.

Rayleigh imaging has been demonstrated [31] to quickly map graphene on a substrate and provide guidance for the optimization of the spacer thickness used to distinguish graphene layers. To make the evaluation quantitative, a contrast spectrum can be obtained much in the same way as absorbance spectroscopy (Fig. 6). From the result, one can estimate the number of layers by comparing it with standard data either directly [32] or through transforming to total color difference values [33].

2.5 Photoluminescence

Similar to Raman spectroscopy, photoluminescence measurements rely on the inelastic scattering of incident light. Differently from Raman scattering, however, this process is not instantaneous, and there is a characteristic delay between illumination of a sample with a light source and reemission of light from the sample. The emission energy is determined by the electronic structure (most commonly the HOMO-LUMO gap) of the sample rather than the energy of the excitation source which allows distinction from Raman effects. Furthermore, photoluminescence is usually significantly stronger than Raman which relaxes requirements on the

Fig. 7 Optical micrograph showing the suppression of fluorescence from defected graphene oxide (*GO*) and higher-quality graphene oxide (*rGO*) (Reproduced with permission from [34])

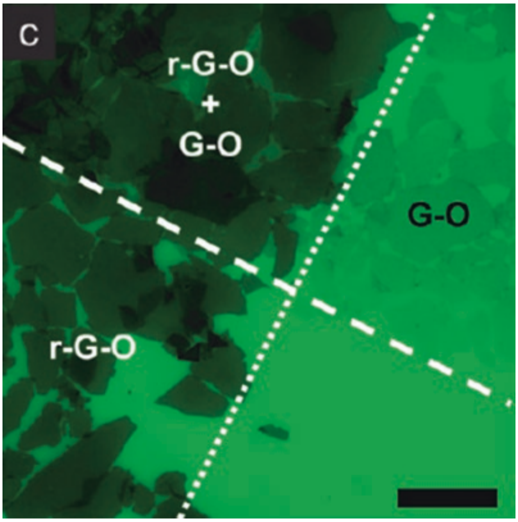

measurement setup. Common measurement setups will have similar layouts as for Raman measurements but allow investigation over a larger range of energy losses. Photoluminescence measurements can be conducted on solid substrates and in liquids, which makes it suitable for many different material types.

Graphene's high electron mobility and semimetallic nature usually impede photoluminescence measurements since photoexcited carriers would relax and recombine before emission takes place. This behavior is exploited in photoluminescence quenching microscopy where the presence of graphene is inferred from the suppression of photoluminescence from neighboring fluorophores (Fig. 7) [34].

Conversely, occurrence of photoluminescence from graphene suggests changes to its electronic structure, and chemical conversion of graphene can be traced by photoluminescence measurements as described later on.

2.6 *Ultrafast Optics*

The characteristic time scales for optical processes reveal important aspects of photoexcitation and carrier relaxation processes. Many of the time-resolved spectroscopy techniques rely on a pump-probe scheme that uses two laser pulses. First, a pulse from a high-intensity laser excites photocarriers or phonons, and then a weaker pulse from a second laser is used to characterize optical properties such as absorption, Raman scattering, or reflection. A variable delay between these two pulses can be used to map out the material's response on the sub-ps time scale. Slower responses can be directly characterized by employing fast detectors.

Ultrafast characterization of liquids, powders, and gasified carbon molecules has been reported [35, 36].

3 Properties

3.1 Thermal Properties

The combination of strong intralayer sp^2 bonds and weak interlayer bonds dictates not only the electrical properties of graphene and related materials but their thermal properties as well. Graphene is predicted to have phenomenal thermal conductivity and heat capacity, giving rise to potential applications such as heat spreaders in nanoelectronics [37]. It is challenging, however, to measure precisely these properties for microscopic objects where defects, boundaries, and substrate interaction can greatly influence the phonon dispersion. Optical techniques have been an enabling tool for nanoscale measurements of thermal properties in graphene.

3.1.1 Raman Spectroscopy

A higher temperature will give rise to a changed average distance between neighboring carbon atoms due to anharmonic terms in the bonding potential. This effect will cause strain in the graphene lattice and can thus be analyzed by Raman spectroscopy as explained later on. The peak position of the G-band was found to blueshift with increasing temperatures according to [38]:

$$\Delta \mathrm{Pos}(G) = -4.23\times10^{-4}T - 3.03\times10^{-5}\,T^2 + 1.15\times10^{-8}T^3$$

A more general approach to determining the temperature of a sample by Raman spectroscopy is to analyze the Stokes and anti-Stokes portion of the Raman spectrum. Since the anti-Stokes Raman requires a phonon for the scattering process to occur, its chance of occurring depends on the amount of present phonons which changes with temperature. Therefore, the ratio of Stokes/anti-Stokes band intensity can be correlated with the temperature according to:

$$\frac{I_{\mathrm{AS}}}{I_S} = \frac{(\nu_l + \nu_v)^4}{(\nu_l - \nu_v)^4} e^{\left(\frac{h\nu_v}{\mathrm{kT}}\right)}$$

where ν_l is the laser frequency (in cm^{-1}) and ν_V is the phonon mode frequency.

Raman spectroscopy proves itself a valuable tool to infer graphene's thermal conductivity. Researchers have advanced an optothermal technique [39] where the strong temperature dependence of G-peak in Raman spectra is used to calculate thermal conductivity. During measurement, a graphene sample of length L and width W is suspended between two heat sinks, and the shifted position of G-peak $\delta\omega$ is monitored with power variation δP. The thermal conductivity is then determined as:

$$K = \chi_G \left(L / 2\mathrm{hW}\right)\left(\delta\omega / \delta P\right)^{-1}$$

where $\chi_G = -1.6\times10^{-2}\mathrm{cm}^{-1}/K$ is the linear temperature coefficient of the G-band shift.

It is noted, however, that many theoretical aspects are not well understood yet, and various experimental factors (sample preparation, laser heating setup) can affect the measurement result. The G-band position is also subject to strain and doping as well, and the interplay between these parameters cannot be neglected (e.g., it is argued that introducing strain can cause irregular change in thermal conductivity) [40].

3.2 Doping

The charge transfer between graphene and its surrounding is a powerful indicator of adsorbates, reactions, charge accumulation, etc. Graphene can act as a charge donor or acceptor which is termed p-doping and n-doping, respectively.

Raman spectroscopy is a useful technique for the characterization of such transfer processes. Intuitively, it is understandable that addition of positive or negative charges will affect the bonding strength of carbon atoms in the lattice and result in a stiffening of the bonds. The resulting blueshift in the resonance frequency can be seen for the G-band of graphene (Fig. 8). The dissimilar trend of the 2D-band position, however, shows the limit of this simple explanation, and more complex interactions between electronic and phononic processes have to be taken into account [41].

In the linear regime of low doping concentrations, the shift can be used to extract the carrier density using the formula [42]:

$$\Delta \mathrm{Pos}(G) = -0.274n^2 + 14.25n$$

Time-dependent perturbation theory at zero temperature was used to arrive at [43]:

$$\hbar\Delta\omega_G = 4.39\times10^{-3}\left|E_F\right|,$$

where $E_F = \hbar v_{\mathrm{Fermi}}\sqrt{\pi n}$.

Importantly, the 2D-band position follows a similar trend with doping for small dopant concentrations, and the two peak shifts are related by [44]:

$$\frac{\Delta\omega_{2D}}{\Delta\omega_G} \sim 0.7$$

The coupling between electronic and phononic states can also be seen when analyzing the intensity of the Raman features. At high doping, all Raman features decrease in intensity, but the decrease with carrier concentration depends on the difference between carrier energy distribution (Fermi energy E_F) and the phonon energy due to Pauli blocking [45].

Therefore, each Raman peak has a distinct intensity variation with doping which depends on its energy, the laser excitation energy, and details of sample stacking and strain. Therefore, intensity ratios, such as the commonly employed 2D/G intensity ratio, should only be compared between similar samples [46].

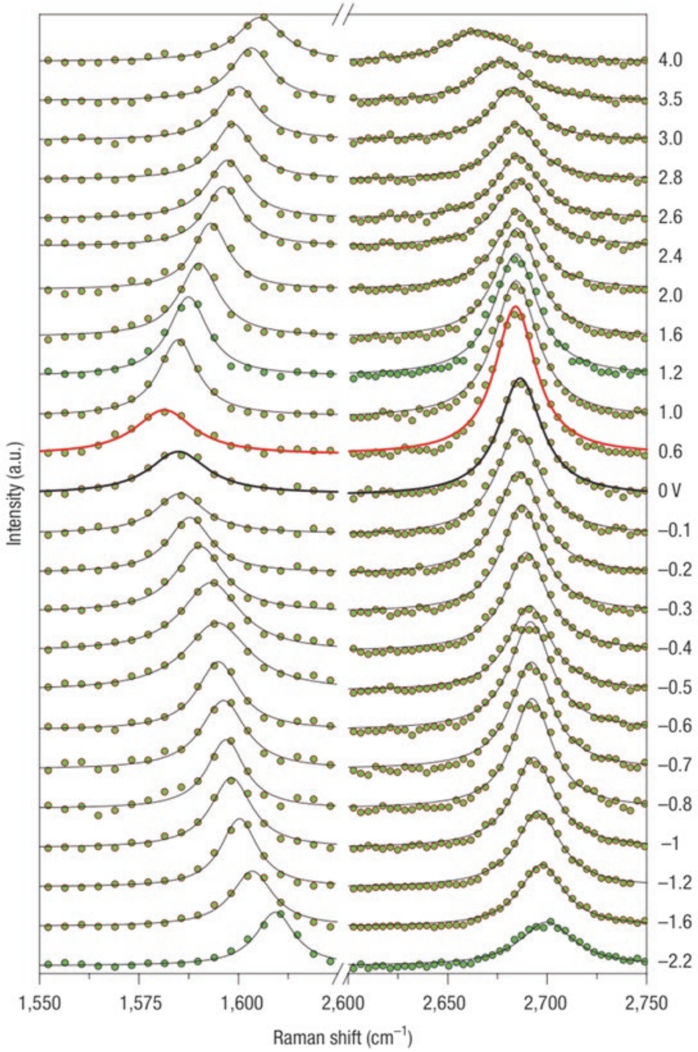

Fig. 8 Impact of doping on the Raman G- and 2D-band [41]. Regions of G-band (*left*) and 2D-band (*right*) are measured across the top gating voltage range -2.2 Volts to 4 Volts, with *red line* undoped condition where the Fermi level intersects the representing the Dirac point (Reproduced with permission from [41])

3.2.1 Absorbance Spectroscopy

An alternative to Raman for extracting the carrier properties of graphene by optical methods is the use of absorbance techniques [47]. Infrared spectroscopy is dominated by two processes. In the far-infrared region (<500 cm^{-1}), absorption is mainly due to free carriers. The absorption of a material at low (angular) frequencies is then determined by the Drude conductivity of graphene according to:

$$A(\omega) = \frac{4\pi}{c}\,\mathrm{Re}\left(\frac{\sigma_0}{1+i\omega\tau}\right)$$

where σ_0 is the DC conductivity of graphene and τ is the electron scattering time [47]. From these two parameters, the Drude weight D can be determined $D = \frac{\pi\sigma_0}{\tau}$ which yields the carrier concentration of graphene n via the relation $D = e^2 v_f \sqrt{\pi n}$, where v_f is the Fermi velocity (1.09×10^6 m/s).

At higher photon energies (>0.1 eV), the absorption is controlled by interband transitions of electrons. The efficiency of this process is determined by the availability of states and can be affected by Pauli blocking of states due to doping. In this situation, the absorptivity takes the form [47]:

$$A(\omega) = \frac{\pi^2 e^2}{\mathrm{hc}}\left[\tanh\left(\frac{\hbar\omega + 2E_F}{4k_BT}\right) + \tanh\left(\frac{\hbar\omega - 2E_F}{4k_BT}\right)\right]$$

where E_F is the Fermi energy that yields the doping concentration $n = E_F^2 / \pi\hbar^2 v_F^2$.

3.2.2 Fast Optics

Another way to probe the carrier concentration of graphene is by characterizing the transient response of electrons to a short pulse (Fig. 9). After excitation, the occupation of the HOMO is smaller than before, while the LUMO occupation is lower

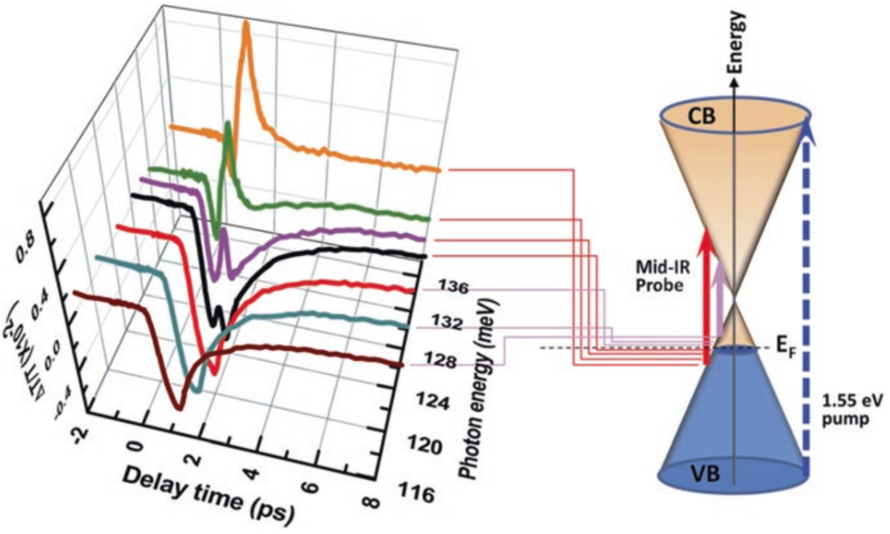

Fig. 9 Time response of transmittance for varying photon energies (Reproduced with permission from [48])

which gives rise to peaks with different signs in the transient spectra. The energy difference between the peaks and the zero-crossing represents the Fermi-level shift relative to the Dirac point and can be used to extract the carrier concentration [48].

Additionally, the time required for photoexcited electrons to decay depends on the efficiency of coupling with phonons. Close to the Fermi level, this effect is smallest and longer decay times are observed. As the probe's excitation energy is increasing beyond the Fermi-level shift, the coupling strength is becoming larger and the decay time shortens. Thus, the decay time's energy dependence can be employed to estimate graphene's carrier occupation [48].

3.3 Strain

The displacement of individual atoms from their equilibrium bond position is an important parameter to evaluate the stability of molecules and crystals. Surprisingly, despite these variations only being in the sub-angstrom range, optical techniques can be employed to analyze even minute changes.

The resonance frequency of phonons as probed by Raman spectroscopy was found to sensitively depend on the strain within a bond, and all Raman features exhibit characteristic shifts in their peak position. The shifts of D-band, G-band, and 2D-band for 1% strain are listed in Table 1 [49, 50].

In the case of uniaxial strain, the G-band splits into two components (G^+ and G^-) whose relative ratio depends on the angle of the laser polarization and the strain axis with respect to the lattice [51]. This ability allows inference to the orientation of the graphene lattice from optical measurements.

The reader is reminded that other factors can affect the position of the Raman features as well, such as temperature and doping.

3.3.1 Infrared Spectroscopy

Infrared spectroscopy is expected to be sensitive to bond deformation, and experimental results on graphene oxide paper indeed show a clear trend of infrared-active phonon mode position with applied strain [52]. Figure 10 shows a negative shift in IR features assigned to C=C and C=O bonds, which maintains linearity up to 1% strain. Challenges in this approach include the low spatial resolution of FTIR and the small peak shift (~2 cm^{-1} per 1% strain) compared to Raman spectroscopy.

Table 1 Overview of Raman shift upon strain in uniaxial and biaxial direction

	G-band	2D-band	D-band
Uniaxial	$-36\ \text{cm}^{-1}$/% strain for G−	$-100\ \text{cm}^{-1}$/% strain	$-50\ \text{cm}^{-1}$/% strain
	$-18\ \text{cm}^{-1}$/% strain for G^+		
Biaxial	$-63\ \text{cm}^{-1}$/% strain	$-200\ \text{cm}^{-1}$/% strain	$-100\ \text{cm}^{-1}$/% strain

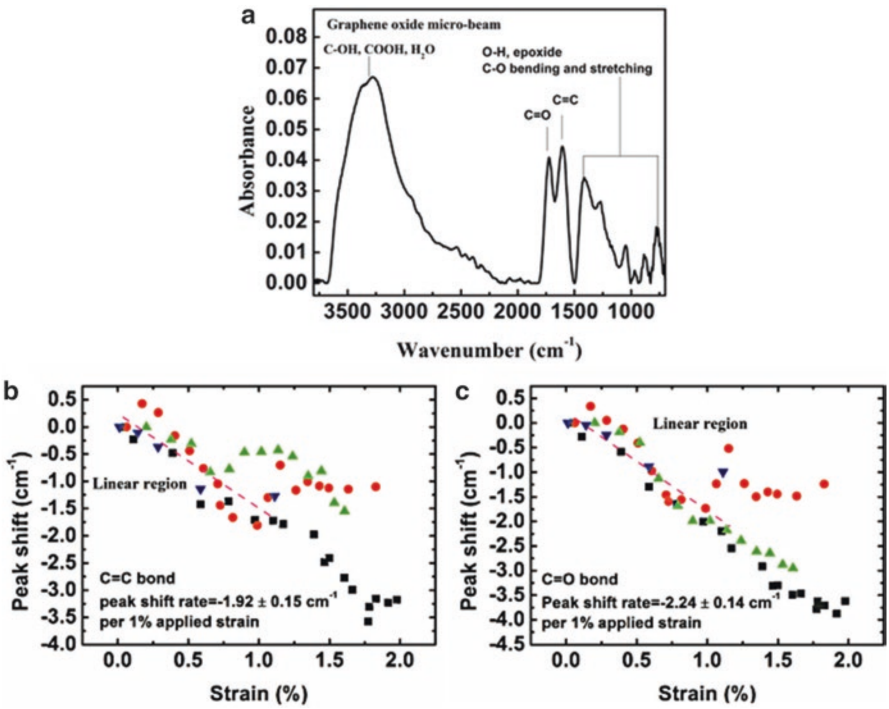

Fig. 10 FTIR spectra of unstrained of graphene oxide (**a**) and peak positions for different amounts of applied strain for C=C (**b**) and C=O (**c**) bonds (Reproduced with permission from [52])

3.4 Thickness and Stacking

Due to different preparation methods and different design purposes, researchers often encounter graphene samples with different thickness and even flakes of various numbers of layers in the same sample. Van-der-Waals interaction between layers, though weak, leads to deviations from the ideal model of graphene as an atomic-thin, two-dimensional crystal and with the number of layers (*n*) increasing the material properties approaches those of bulk graphite. It is evaluated that only the materials constituted of less than ten layers [53] retain some properties from monolayer graphene and have been qualified as “few-layer graphene.” Thus, it is important to determine the thickness of prepared graphene.

While the thickness of graphene can be observed through electron and scanning probe microscopy techniques, they are usually slow and potentially damaging to the sample. Similar information can be conveniently obtained by nondestructive optical methods. The decrease of optical transmittance is a powerful indicator of a thickness increase. It is found that [6] at 550 nm wavelength, the transmittance is mostly independent of stacking order and correlated with the number of layer by a relatively simple equation:

$$T(\omega) = \left(1 + f(\omega)\pi\alpha \times n/2\right)^{-2}$$

where α is the fine structure constant and $f(\omega)$ is a correction coefficient, which can be used to determine the thickness up to tens of layers.

Optical microscopy can determine the thickness as well, by exploiting the contrast difference in Rayleigh scattering image [31] or fluorescent quenching image [54] (Fig. 11). Compared with spectroscopy methods, these techniques are more versatile in evaluating sample in larger scale (up to cm size), but not without flaws. Contrast in fluorescence was found to saturate for samples with $n \geq 3$, while reflectance is strongly influenced by background, and therefore Rayleigh imaging can be realized only with appropriate substrate of precise thickness (300 nm SiO_2 layer, with anti-reflectance coating). Recently, interference reflection microscopy – a derivative of fluorescence microscopy – proved able to image graphene layers with outstanding contrast [55] even on transparent substrates typically challenging for the other techniques.

The perpendicular arrangement of graphene layers forms weakly bonded van der Van-der-Waals solids that are akin to pi-stacking in organic chemistry. This stacking will change the electronic structure and limit interaction of inner-lying layers with the environment. Furthermore, the effect of the stack size in the transition between graphenic and graphitic properties enhances our understanding of nanoscale confinement effects.

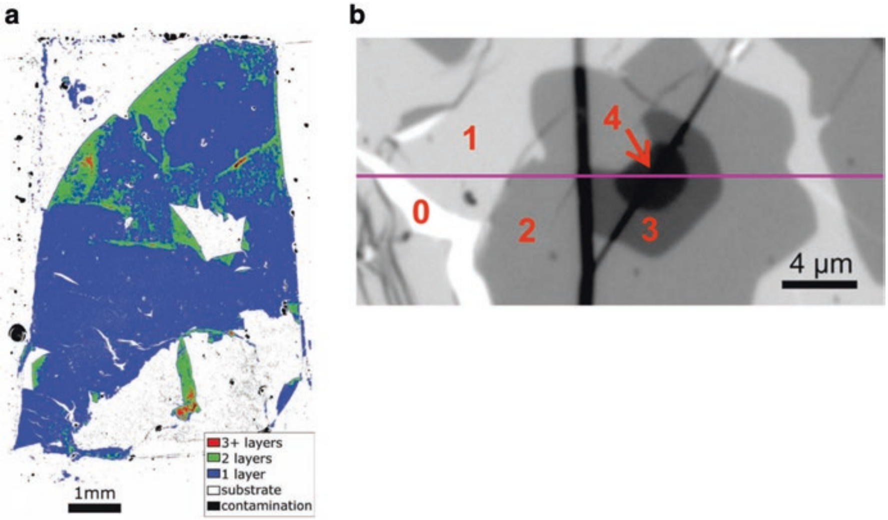

Fig. 11 Layer identification by fluorescence quenching microscopy (*left*) [54] and interference reflection microscopy (*right*) (Reproduced with permission from [55])

Both the phononic and electronic interaction of stacked graphene layers are sensitive to the number and alignment of adjacent layers that can be detected by optical means.

Since Raman spectroscopy allows characterization of both interactions, it is expected that Raman will be a powerful method to analyze stacks.

As will be discussed later on, graphene's 2D-band is enhanced by resonance effects. This process will selectively enhance phonons with energy and momentum values that can match graphene's band structure. Thus, small changes in graphene's band structure will result in the selection of different phonons. For single-layer graphene, only one phonon can satisfy the scattering conditions, and the 2D-band only consists of one peak. As the graphene stack becomes thicker, more electronic states occur and more phonons can contribute to the scattering. Thus, the 2D-band is composed of more peaks, and deconvolution will allow inference to the thickness [56]. We have to note, however, that changes in graphene's defectiveness will also affect the 2D peak width (as discussed later on), and care has to be taken to account for such modifications, e.g., by comparing stacks of graphene of similar defectiveness.

The interaction of more graphene layers in a stack will produce new bonds and thus new phonons that create additional bands in the Raman spectrum.

The shear mode (or C mode) has very weak bond strengths and thus occurs at low energies (around 40 cm^{-1}) that are not easily accessible by Raman setups. However, its position change with the number of layers is a good indicator of the graphene stack size for a wide range of layer numbers N:

$$\mathrm{Pos}(C)_N = \sqrt{\frac{2\alpha}{\mu}\sqrt{1+\cos\left(\frac{\pi}{N}\right)}}$$

where $\alpha = 12.8\times10^{18} N\ \mathrm{m}^{-3}$ is the interlayer coupling and $\mu = 7.6\times10^{-7}\mathrm{kg\ m}^{-2}$is the graphene mass per unit area [28].

Additionally, weak higher energy bands between 1650 and 2300 cm^{-1}, called "combination modes," show interaction between adjacent layers. These bands include the M band around 1750 cm^{-1} which only occurs for strongly coupled layers and is activated by scattering with two out-of-plane optical phonons [57]. Other phonon modes represent combinations between in-plane and out-of-plane modes, and their intensity reveals information on the coupling between atoms in neighboring layers [58] (Fig. 12).

When adjacent graphene layers do not perfectly align with each other, the result is twisted bilayer graphene that forms a Moiré pattern (Fig. 13). The electronic structure of twisted bilayer graphene is more complicated than that of the more well-known AB-stacked graphene, with a Fermi velocity slower than in the latter (and much slower than in single-layer graphene) and an electronic structure depending on the angle θ between two layers [59].

The most prominent feature of Raman spectra in twisted bilayer graphene is a G-band enhancement that is dependent on the twist angle θ and the laser energy. The G-band intensity will increase with increasing rotation angle until it reaches a peak at a critical angle θ_c related to the excitation energy E_{laser} by the resonance condition [60]:

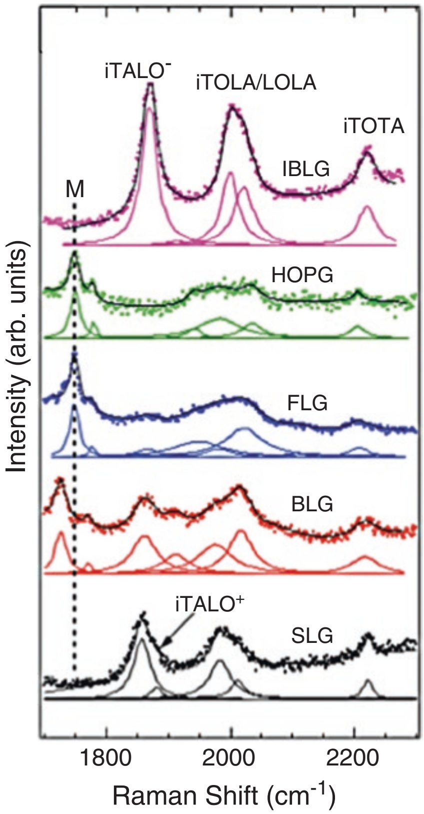

Fig. 12 Representative Raman spectra showing combination modes (top) and their relative strength for different carbon systems, i.e. from bottom to top: Single layer graphene, bilayer graphene, few layer graphene, and highly oriented pyrolytic graphite (Reproduced with permission from [57])

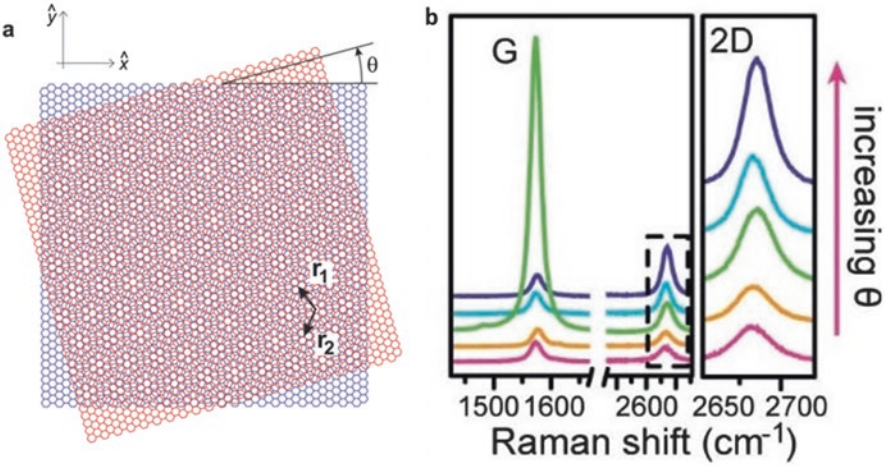

Fig. 13 (**a**) Moiré pattern of graphene superlattice (Reproduced with permission from [61]) (**b**) G- and 2D-Raman features as a function of twisting angle (Reproduced with permission from [62])

$$\theta_c = (\Delta \mathrm{k}/k)/(K) = 3aE_{\mathrm{laser}} / \hbar \upsilon_f 4\pi$$

where a is the lattice parameter (2.46 Å) and υ_f is the Fermi velocity of monolayer graphene (10^6m/s).

Therefore, energy-tunable Raman spectroscopy can be used to determine the rotation angle [62].

The lattice mismatch is also reflected in the complex evolution in the 2D-band intensity, the occurrence of new rotation-induced R- and R′-bands [61], and the splitting of the C mode [63] which, as mentioned above, is often difficult to observe experimentally. Similarly, twisting is predicted to change graphene's optical absorption significantly [64], but aside from the contrast spectra that can be used to locate folded graphene layer, little quantitative work has been carried in this aspect.

When a third layer is added to an AB bilayer graphene, the result can be ABA (Bernal stacking) or ABC (rhombohedral stacking) configurations. The former retains semimetallic characteristics, while the latter resembles a semiconductor with tunable bandgap [65]. There are subtle differences between Raman spectra of the two stacking order, most notably a broader and more asymmetric 2D-band in ABC stacking. By fitting the 2D-band to Lorentzian function for each pixel, it is possible to map the regions with different stacking orders [66]. To rule out the effects of other factors like strain and disorder on the 2D bandwidth, the evaluation can be reinforced by supplementary information from G-band (narrower in ABC) and intermediate frequency modes (1690–2150 cm^{-1}) [67]. Differences between the two types of stacking are also observed in infrared optical conductivity [68], but the measurement requires specialized equipment working in low temperature and provides lower resolution.

3.5 Defectiveness

Deviations from the perfect sp2 lattice of graphene are the source of increased reactivity, changes in fundamental properties, and exciting applications. From the here employed simple description, however, they are considered defects, and several techniques exist to identify and quantify them.

Raman spectroscopy of defective graphene shows additional peaks compared to its pristine counterpart. As previously mentioned, the D-band is a Raman active phonon mode of A1g symmetry. However, this mode requires an external momentum to be excited. Since light does not have an appreciable momentum, the D-band can only be excited if momentum originates from another source. One such source is a discontinuity in the graphene lattice where some bonds to neighboring carbon atoms are broken. In such a situation, the defect reverses the direction of phonon propagation, and no overall momentum is required to excite the phonon.

Therefore, the D-band will only occur in the presence of defects, and its intensity will change with their concentration. Unfortunately, this dependence is not direct. Instead, the D-band intensity will first increase with defectiveness at low defect concentrations and then decrease with defectiveness at high defect concentrations.

One can understand this behavior by considering the origin of the D-band peak. At low defect concentration, the D-band reflects the concentration of defects because a large population of A1g phonons is available. However, as more and more defects occur, the D-band intensity becomes limited by the number of phonons that originate from the motion of undefected carbon hexagons. Thus, the D-band is an indicator of disorder at low defect concentration but becomes a measure of order for high defect concentrations.

Lucchese et al. [69] have quantitatively described the complete trend of the D-band intensity as normalized by the G-band intensity (ID/IG), which follows the formula:

$$\frac{I_D}{I_G} = \frac{C_A\left(r_A^2 - r_S^2\right)}{r_A^2 - 2r_S^2}\left[e^{-\frac{\pi r_S^2}{L_D^2}} - e^{-\pi\left(r_A^2 - r_S^2\right)/L_D^2}\right] + C_s\left[1 - e^{-\frac{\pi r_S^2}{L_D^2}}\right]$$

where L_D is the average size of a defect cluster. The parameters C_A, C_S, r_A, and r_S were obtained from a fit of experimental data and were found to be $C_A = 4.2$, $C_S = 0.87$, $r_A = 3$nm, and $r_S = 1$nm.

This description was further improved by extracting a quantitative relation between the I_D/I_G ratio and the defect concentration as a function of laser excitation wavelength λ_L in the region of low defect concentration [70] (see Fig. 14):

$$n_D\left(\mathrm{cm}^{-2}\right) = \frac{1.8 \times 10^{22}}{\lambda_L^4}\left(\frac{I_D}{I_G}\right)$$

where λ_L is the wavelength in nm.

At low defect concentrations, an additional Raman band will occur. This feature is termed the D′-band and originates from an out-of-phase longitudinal displacement with small momentum [27]. While the D′ intensity increases with defect den-

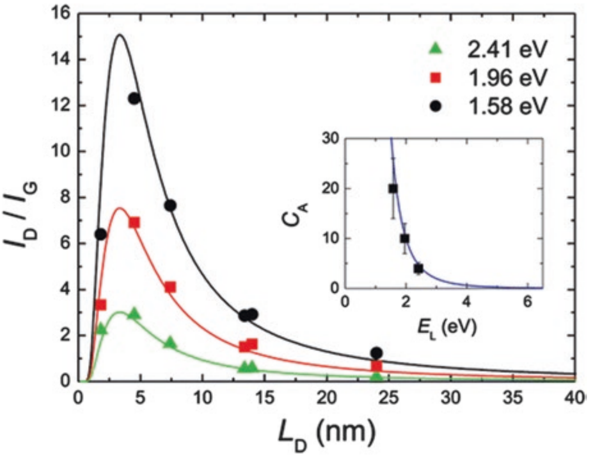

Fig. 14 Raman I_D/I_G ratio for different laser wavelengths as a function of defect cluster size (Reproduced with permission from [70])

sity as well, it requires defects that produce little momentum to satisfy the momentum conservation upon interaction with light. Therefore, it is activated by defects with different properties than the D-band, and the comparison of D′- and D-band intensity allows inference to the types of defects (Fig. 15). It was observed that sp^3-type defects show a significantly higher $I_D/I_{D'}$ ratio (~13) than vacancies (~7) and boundaries (~3.5) [71].

Raman spectroscopy can provide additional information on the type of boundary-type defects due to their relatively long-range order. It was found that armchair edges produce a lower D-band intensity than boundaries formed from zigzag edges [72]. Furthermore, a polarization perpendicular to an edge produces a low D-band intensity than parallel to an edge [72].

One further feature that is normally overlooked in the analysis of graphene's defectiveness is the width of the Raman feature. Intuitively, the increasing heterogeneity in the bonding character around defects can be thought to produce a variability in a bond resonance frequency. This simple explanation does not consider the shortened lifetime of electrons or different coupling strengths of electrons and phonons in the presence of defects, but in general a larger peak width is associated with a higher defectiveness [73].

3.5.1 Infrared Spectroscopy

In spite of the rise of other techniques like NMR, mass spectroscopy, and XRD in chemical analysis, FTIR is still favored as a low-cost, versatile tool to elucidate the chemical nature of defects. The identification of functional groups can be conveniently done by looking up the bands of FTIR spectra in well-established correlation tables. If a polarized light source is employed, one can determine the orientation of the functional group and then infer its local distribution [74]. More quantitative

Fig. 15 Difference in D′-band intensity for two different types of defected graphene (Reproduced with permission from [71])

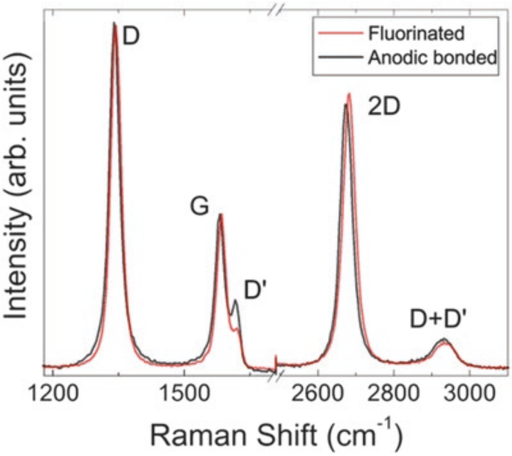

analysis will require a comprehensive understanding of graphene's IR spectra. As of now, attempts at such model using DFT calculations are still inadequate, generating uncertainty of tens of cm^{-1} at best [19].

3.5.2 Photoluminescence

As mentioned earlier, pristine graphene does not exhibit photoluminescence due to the fast non-radiative relaxation of photoexcited carriers. Therefore, the occurrence of photoluminescence is a strong indication for increased graphene defectiveness. Several mechanisms for PL emission have been identified [75].

Localized modifications of the graphene basal plane, for example, could result in domains that emit light due to changes in the band structure (Fig. 13). Their emission properties could be further modified through geometric confinement effects. Ab initio simulations suggest a clear trend between apparent bandgap and emissive domain size with 20 aromatic rings exhibiting a bandgap of approximately 2 eV and 100 aromatic rings having 0.5 eV [76].

Alternatively, interaction with chemical groups can produce luminescent centers. These types of defects were reported to produce the strongest emission [77]. Indeed, as demonstrated in Fig. 16, strong quenching of emission has been observed after processing was conducted that aimed at decreasing graphene's defect concentration [78]. Moreover, pH dependence of graphene's fluorescence suggests that these luminescent centers are quasi-molecular in nature [79].

3.6 Electronic Structure

3.6.1 Raman

Surprisingly, Raman spectroscopy has proven a very useful tool for the identification of the band structure of one of graphene's derivatives – carbon nanotubes [81]. A resonance effect was observed to dramatically increase the Raman intensity when the laser excitation source matches the electronic band structure. This effect was explained by the increased chance of transitioning between two electronic states in the band structure compared to the chance of transitioning to a mixture of states called "virtual" where momentum conservation has to be satisfied for each contributing state. Consequently, Raman scattering mainly originates from nanotubes with suitable band structure that allows access to the Raman response of different constituents of a distribution using different excitation [82].

The same resonance effect can be found in graphene, whose accessible electronic band structure does not span as large of an energy range as in semiconductors that possess large bandgaps.

The 2D-band is a second-order scattering effect where two phonons of equal magnitude and opposite propagation direction have to be created simultaneously to

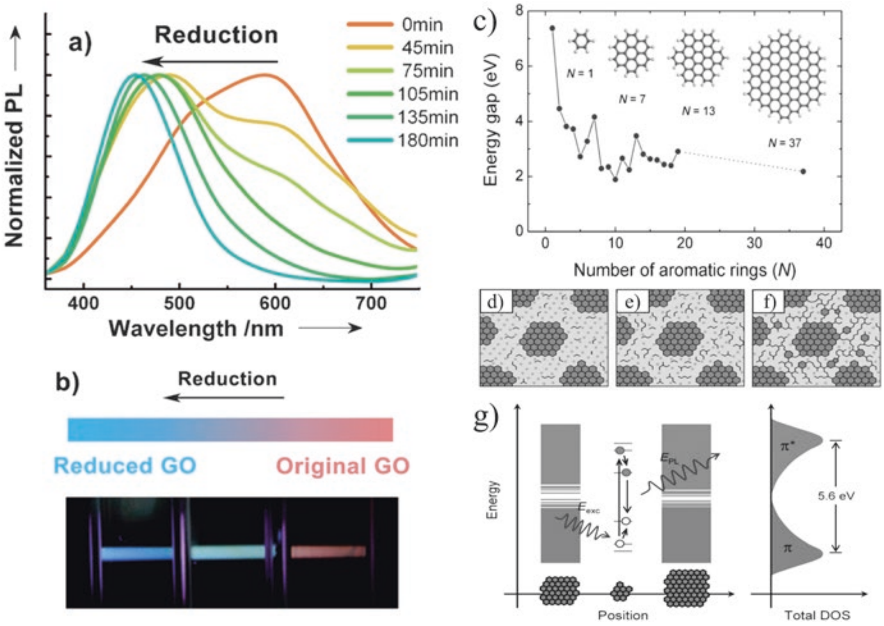

Fig. 16 (a) Photoluminescence spectra of defected graphene after varying reduction time, (b) photograph of luminescence color for varying graphene oxide reduction. (Reproduced with permission from [80]) and (c) Simulated band gaps for graphenic regions with different dimensions, (d-f) schematic of distribution of defects and (g) corresponding energy diagrams (Reproduced with permission from [76])

satisfy the momentum conservation condition mentioned above. Such a coincidence of steps is commonly very unlikely, and second-order effects are significantly weaker than first-order Raman features. Instead, the 2D-band is usually the largest feature of the graphene Raman spectrum (Fig. 5). This difference is due to a double resonance effect between electronic and phononic interaction. Light excitation will generate electrons in real states that are usually scattered by a phonon to a virtual state. In the case of the 2D-band, however, two A1g phonons connect the initial state to two more real states. This resonance enhancement increases the scattering efficiency so much that even a second-order process is discernable. Consequently, graphene's band structure can be analyzed by the 2D-band intensity and position.

The 2D-band intensity is affected by the availability of electronic states that allow scattering. Therefore, the absence of a 2D-band is an indication of disruptions of graphene's band structure. Such changes can be produced by opening a significant bandgap due to confinement into nano-ribbons or quantum dots [83, 84]. Indeed Raman spectroscopy shows marked variations in their 2D-band intensity, and the polarization dependence can be employed to infer the geometry of the confinement [72].

Unfortunately, the 2D-band intensity is related only to scattering that occur far away from the equilibrium energy levels and is not indicative of more subtle changes to graphene's band structure, such as the opening of mini-gaps or the modification of the bands in multilayer graphene.

Here, the analysis of the position and components of the 2D-band can help. Since resonance can occur between different parts of the band structure, different phonon energies are required to connect those states. Consequently, changes in the phonon energy are an indication of different resonance conditions occurring. One important example of such a process is the change in graphene's thickness and stacking as discussed earlier.

Energy-tunable Raman scattering where the position of Raman features is characterized for different excitation energies can reveal changes to graphene's electronic structure with high sensitivity. For example, hydrogen absorption was found to produce changes in the electronic structure that cause an excitation energy dependent red shift of D- and 2D-bands [85].

Confinement effects for ultra-narrow graphene nanoribbons (<2 nm) not only produce new Raman features associated with the collective displacement of the crystal in a breathing-like pattern but also changes its energy dispersive behavior [86] (Fig. 17). The D-band of such nanoribbons was found to exhibit a different dispersion for low and high excitation energies neither of which agrees with the slope of infinite graphene. This behavior was related to the formation of bandgaps and the relaxation of momentum conservation rules [86].

3.6.2 Photoluminescence

Photoluminescence measurements are commonly employed to elucidate the electronic structure of molecules and nanostructures. In the case of graphene, photoluminescence is caused by defects (see above) as well as global modification of the graphene structure. For example, the oxidation of graphene will produce new localized states in its band structure. Due to momentum selection, decay from those states will proceed by emission rather than non-radiative relaxation as is the case for pristine graphene [87]. Theoretical calculations are aiming at quantifying the relation between oxygen concentration and the thus opened energy gap [88].

3.6.3 Infrared Spectroscopy

Infrared spectroscopy provides a direct way to identify small changes in the band structure since the excitation energy is low enough to probe even small energy gaps. A common method to identify such changes in graphene's band structure is by detecting deviations from the ideal model. Electrons in ideal graphene behave like massless Dirac fermions, and pristine graphene's IR response can be approximated by the Drude model, with its time constant corresponds to the infrared frequency range. In this range, the Drude conductivity [7] is related to free-carrier scattering rate Γ and Drude weight D:

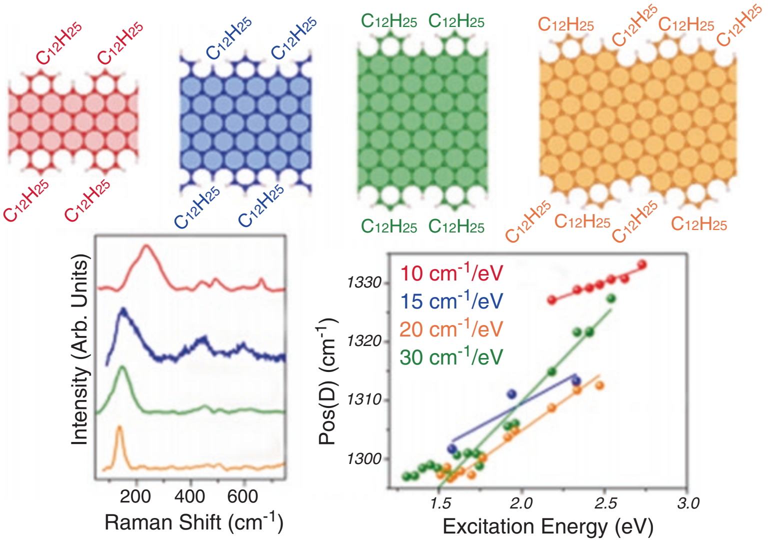

Fig. 17 Raman spectra of atomically precise nanoribbons with different structures and their energy dispersion (Reproduced with permission from [86])

$$\sigma(\omega) = \frac{iD}{\pi(\omega + i\Gamma)}$$

The sheet conductivity can be calculated from the reduction in transmission:

$$1 - {T}/{T_0} = \frac{1}{\left|1 + Z_0\sigma(\omega)/(1+n_s)\right|^2}$$

where $Z_0 = (\mu_0/\epsilon_0)^{1/2}$ is vacuum impedance and $n_s$is the substrate's refractive index.

When analyzing the Drude conductivity of a bilayer graphene sample in a strong perpendicular electric field, characteristic peaks were found (Fig. 18), [89]. These peaks around 0.4 eV and 0.3 eV indicated transition across the bandgap or two states in the conduction band, respectively. A clear dependence on the strength of the applied perpendicular field confirmed the electric field-induced bandgap in bilayer graphene.

3.6.4 Ultrafast Optics

For an understanding of carrier relaxation processes that happen in transient time scales, time-resolved spectroscopy is needed. With optical excitation in the infrared range, two distinct decay times are observed in the differential transmission spectra:

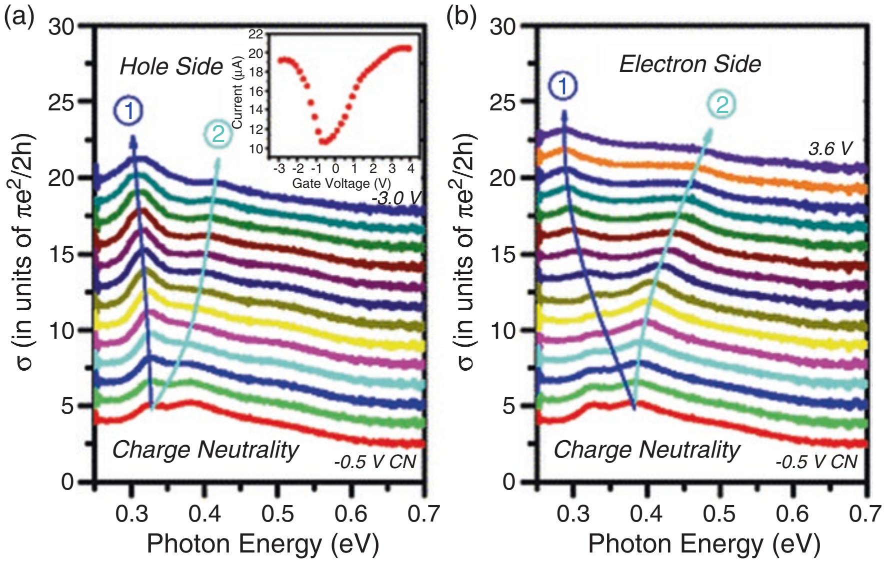

Fig. 18 Extracted spectral sheet conductivity in bilayer graphene as a function of applied perpendicular field (Reproduced with permission from [89])

the first, at femtosecond scale, is characteristic of carrier thermalization, and the second, at sub-picosecond scale, is caused by carrier cooling, though the measured time constants are varied slightly between studies [90]. Ultrafast infrared spectroscopy has been used to extract Fermi level and other carrier properties in doped layers and deduce the effect of screening by these layers [91].

3.7 Distinction of Effects and Combination of Techniques

The presented examples show the power of optical spectroscopy but also reveal shortcomings. Several effects can simultaneously affect an optical process and cannot be distinguished from single measurements.

A common approach to clarifying the origin of changes to one optical process is the combination of several techniques on one sample. Since several techniques can provide complementary information on one property, clearer information on this aspect can be obtained.

For example, a combination of FTIR spectroscopy and Raman I_D/I_G ratio is routinely used to elucidate the quality of graphene [92]. Furthermore, graphene thickness can be assessed using optical contrast measurements which are relatively quick, while accurate calibration is only carried out on a few samples using Raman spectroscopy [93].

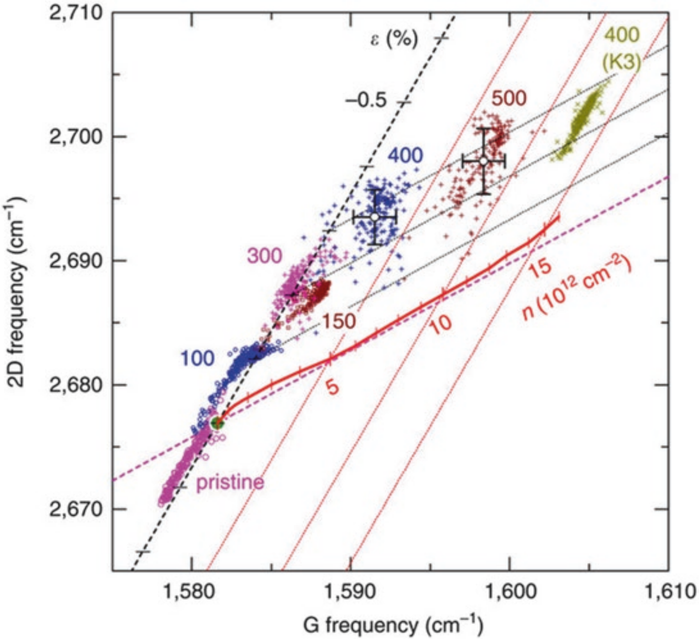

Fig. 19 Scaling analysis of 2D-band and G-band position for graphene after different heat treatments (Reproduced with permission from [44])

A more sophisticated variant of combining multiple optical techniques is hyperspectral imaging. This approach allows investigation of several optical features at the same location. Combination of UV and visible spectroscopy techniques, for example, revealed the mapping of twist angle and chemical makeup in stacks of bilayer graphene and boron nitride monolayers with high spatial resolution [94].

Alternatively, combination of optical techniques at the same time can reveal subtle changes during processing. Simultaneous analysis of the Raman D/G ratio and the 2D-band position during UV exposure allowed investigation of the charge transfer in graphene due to oxidation while accounting for defect-induced property changes [95].

While the combination of spectroscopic techniques is a powerful approach, suitable experimental setups are not widely available. One elegant approach to extract meaningful data from one measurement is through scaling analysis. Lee et al. [44], for example, could distinguish the effects of temperature-induced strain and doping on graphene Raman spectra (Fig. 19). Since both processes affect the position of the G-band and the 2D-band in a different way, they analyzed the trends in position for a large number of Raman spectra. As explained earlier, the 2D-band position should 2.2 times as much as the G-band position for changes in strain, whereas it should only shift 0.7 times when the doping changes. It was found that the observed change was a mixture of both effects, and an eigenvalue decomposition was used to infer the contribution of strain and doping to each spectrum [96].

4 Conclusion

In this contribution, we attempted to give an overview of the wealth of complementary information about graphene that can be revealed by optical spectroscopy techniques. Atomic processes and subtle changes in properties provide clear signatures that allow destruction-free and facile characterization using widely available methods. The relatively simple structure and high quality of graphene makes this material ideally suitable to investigate the complex relation between geometry, electronic properties, and optical characteristics. Many lessons that were learned from graphene can be applied to the characterization of complex molecules. Moreover, compatibility of optical characterization techniques with high reaction temperature and pressures commonly observed in Suzuki reactions enables in situ measurements of bond formation [97]. Obtained Raman spectra show characteristic peaks that originate from similar phonon modes as in graphene, and analysis of their intensity can reveal the mechanism and reaction kinetics of chemical reactions [98].

While these results establish a similarity between complex molecules and graphene, we hope that these research areas can provide new impulses to each other in the future.

References

1. S. Kotha, K. Lahiri, D. Kashinath, Recent applications of the Suzuki-Miyaura cross-coupling reaction in organic synthesis. Tetrahedron **58**, 9633–9695 (2002)
2. V. Georgakilas, M. Otyepka, A.B. Bourlinos, V. Chandra, N. Kim, K.C. Kemp, P. Hobza, R. Zboril, K.S. Kim, Functionalization of graphene: covalent and non-covalent approaches, derivatives and applications. Chem. Rev. **112**, 6156–6214 (2012)
3. R.R. Nair, P. Blake, A.N. Grigorenko, K.S. Novoselov, T.J. Booth, T. Stauber, N.M.R. Peres, A.K. Geim, Fine structure constant defines visual transparency of graphene. Science **320**, 1308–1308 (2008)
4. J.M. Dawlaty, S. Shivaraman, J. Strait, P. George, M. Chandrashekhar, F. Rana, M.G. Spencer, D. Veksler, Y. Chen, Measurement of the optical absorption spectra of epitaxial graphene from terahertz to visible. Appl. Phys. Lett. **93**, 131905 (2008)
5. V.G. Kravets, A.N. Grigorenko, R.R. Nair, P. Blake, S. Anissimova, K.S. Novoselov, A.K. Geim, Spectroscopic ellipsometry of graphene and an exciton-shifted van Hove peak in absorption. Phys. Rev. B **81**, 155413 (2010)
6. Z. Shou-En, Y. Shengjun, G.C.A.M. Janssen, Optical transmittance of multilayer graphene. EPL (Europhys Lett.) **108**, 17007 (2014)
7. H. Yan, F. Xia, W. Zhu, M. Freitag, C. Dimitrakopoulos, A.A. Bol, G. Tulevski, P. Avouris, Infrared spectroscopy of wafer-scale graphene. ACS Nano **5**, 9854–9860 (2011)
8. K.F. Mak, F.H. da Jornada, K. He, J. Deslippe, N. Petrone, J. Hone, J. Shan, S.G. Louie, T.F. Heinz, Tuning many-body interactions in graphene: the effects of doping on excitons and carrier lifetimes. Phys. Rev. Lett. **112**, 207401 (2014)
9. A. Matković, M. Chhikara, M. Milićević, U. Ralević, B. Vasić, D. Jovanović, M.R. Belić, G. Bratina, R. Gajić, Influence of a gold substrate on the optical properties of graphene. J. Appl. Phys. **117**, 015305 (2015)

10. C. Lee, N. Leconte, J. Kim, D. Cho, I.-W. Lyo, E.J. Choi, Optical spectroscopy study on the effect of hydrogen adsorption on graphene. Carbon **103**, 109–114 (2016)
11. J.I. Paredes, S. Villar-Rodil, A. Martínez-Alonso, J.M.D. Tascón, Graphene oxide dispersions in organic solvents. Langmuir **24**, 10560–10564 (2008)
12. D. Li, M.B. Muller, S. Gilje, R.B. Kaner, G.G. Wallace, Processable aqueous dispersions of graphene nanosheets. Nat Nano **3**, 101–105 (2008)
13. J. Zhang, H. Yang, G. Shen, P. Cheng, J. Zhang, S. Guo, Reduction of graphene oxide vial-ascorbic acid. Chem. Commun. **46**, 1112–1114 (2010)
14. N. Kurantowicz, E. Sawosz, S. Jaworski, M. Kutwin, B. Strojny, M. Wierzbicki, J. Szeliga, A. Hotowy, L. Lipińska, R. Koziński, J. Jagiełło, A. Chwalibog, Interaction of graphene family materials with *Listeria monocytogenes* and Salmonella enterica. Nanoscale Res. Lett. **10**, 1–12 (2015)
15. P. Larkin, Chapter 3: Instrumentation and sampling methods, in *Infrared and Raman Spectroscopy*, (Elsevier, Oxford, 2011), pp. 27–54
16. H.-L. Guo, X.-F. Wang, Q.-Y. Qian, F.-B. Wang, X.-H. Xia, A green approach to the synthesis of graphene nanosheets. ACS Nano **3**, 2653–2659 (2009)
17. J. O'reilly, R. Mosher, Functional groups in carbon black by FTIR spectroscopy. Carbon **21**, 47–51 (1983)
18. C. Hontoria-Lucas, A.J. López-Peinado, J.D.D. López-González, M.L. Rojas-Cervantes, R.M. Martín-Aranda, Study of oxygen-containing groups in a series of graphite oxides: physical and chemical characterization. Carbon **33**, 1585–1592 (1995)
19. C. Zhang, D.M. Dabbs, L.-M. Liu, I.A. Aksay, R. Car, A. Selloni, Combined effects of functional groups, lattice defects, and edges in the infrared spectra of graphene oxide. J. Phys. Chem. C **119**, 18167–18176 (2015)
20. A. Kaniyoor, T.T. Baby, S. Ramaprabhu, Graphene synthesis via hydrogen induced low temperature exfoliation of graphite oxide. J. Mater. Chem. **20**, 8467–8469 (2010)
21. S. Eigler, C. Dotzer, A. Hirsch, M. Enzelberger, P. Müller, Formation and decomposition of CO2 intercalated graphene oxide. Chem. Mater. **24**, 1276–1282 (2012)
22. X. Wang, W. Wang, Y. Liu, M. Ren, H. Xiao, X. Liu, Characterization of conformation and locations of C–F bonds in graphene derivative by polarized ATR-FTIR. Anal. Chem. **88**, 3926–3934 (2016)
23. Y. Si, E.T. Samulski, Synthesis of water soluble graphene. Nano Lett. **8**, 1679–1682 (2008)
24. S. Konwer, J.P. Gogoi, A. Kalita, S.K. Dolui, Synthesis of expanded graphite filled polyaniline composites and evaluation of their electrical and electrochemical properties. J. Mater. Sci. Mater. Electron. **22**, 1154–1161 (2011)
25. I. Milosevic, N. Kepcija, E. Dobardzic, M. Mohr, J. Maultzsch, C. Thomsen, M. Damnjanovic, Symmetry-based analysis of the electron-phonon interaction in graphene. Physica Status Solidi B-Basic Solid State Phys. **246**, 2606–2609 (2009)
26. S. Reich, C. Thomsen, Raman spectroscopy of graphite. Philos. Trans. R. Soc. A Math. Phys. Eng. Sci. **362**, 2271–2288 (2004)
27. J.F. Rodriguez-Nieva, E.B. Barros, R. Saito, M.S. Dresselhaus, Disorder-induced double resonant Raman process in graphene. Phys. Rev. B **90**, 235410 (2014)
28. A.C. Ferrari, D.M. Basko, Raman spectroscopy as a versatile tool for studying the properties of graphene. Nat. Nanotechnol. **8**, 235–246 (2013)
29. F. Schedin, E. Lidorikis, A. Lombardo, V.G. Kravets, A.K. Geim, A.N. Grigorenko, K.S. Novoselov, A.C. Ferrari, Surface-enhanced Raman spectroscopy of graphene. ACS Nano **4**, 5617–5626 (2010)
30. D.Y. Joh, L.H. Herman, S.-Y. Ju, J. Kinder, M.A. Segal, J.N. Johnson, G.K.L. Chan, J. Park, On-chip Rayleigh imaging and spectroscopy of carbon nanotubes. Nano Lett. **11**, 1–7 (2011)
31. C. Casiraghi, A. Hartschuh, E. Lidorikis, H. Qian, H. Harutyunyan, T. Gokus, K. Novoselov, A. Ferrari, Rayleigh imaging of graphene and graphene layers. Nano Lett. **7**, 2711–2717 (2007)
32. Z. Ni, H. Wang, J. Kasim, H. Fan, T. Yu, Y. Wu, Y. Feng, Z. Shen, Graphene thickness determination using reflection and contrast spectroscopy. Nano Lett. **7**, 2758–2763 (2007)

33. L. Gao, W. Ren, F. Li, H.-M. Cheng, Total color difference for rapid and accurate identification of graphene. ACS Nano **2**, 1625–1633 (2008)
34. J. Kim, L.J. Cote, F. Kim, J.X. Huang, Visualizing graphene based sheets by fluorescence quenching microscopy. J. Am. Chem. Soc. **132**, 260–267 (2010)
35. J.Z. Shang, L. Ma, J.W. Li, W. Ai, T. Yu, G.G. Gurzadyan, Femtosecond pump-probe spectroscopy of graphene oxide in water. J. Phys. D-Appl. Phys. **47**, 173106 (2014)
36. C. Schriever, S. Lochbrunner, E. Riedle, D.J. Nesbitt, Ultrasensitive ultraviolet-visible 20 fs absorption spectroscopy of low vapor pressure molecules in the gas phase. Rev. Sci. Instrum. **79**, 013107 (2008)
37. D.J. Renteria, L.D. Nika, A.A. Balandin, Graphene thermal properties: applications in thermal management and energy storage. Appl. Sci. **4**, 525–547 (2014)
38. N. Rotenberg, L. Kuipers, Mapping nanoscale light fields. Nat. Photonics **8**, 919–926 (2014)
39. A.A. Balandin, S. Ghosh, W. Bao, I. Calizo, D. Teweldebrhan, F. Miao, C.N. Lau, Superior thermal conductivity of single-layer graphene. Nano Lett. **8**, 902–907 (2008)
40. L. Lindsay, W. Li, J. Carrete, N. Mingo, D.A. Broido, T.L. Reinecke, Phonon thermal transport in strained and unstrained graphene from first principles. Phys. Rev. B **89**, 155426 (2014)
41. A. Das, S. Pisana, B. Chakraborty, S. Piscanec, S.K. Saha, U.V. Waghmare, K.S. Novoselov, H.R. Krishnamurthy, A.K. Geim, A.C. Ferrari, A.K. Sood, Monitoring dopants by Raman scattering in an electrochemically top-gated graphene transistor. Nat. Nanotechnol. **3**, 210–215 (2008)
42. T.G.A. Verhagen, K. Drogowska, M. Kalbac, J. Vejpravova, Temperature-induced strain and doping in monolayer and bilayer isotopically labeled graphene. Phys. Rev. B **92**, 125437 (2015)
43. S. Pisana, M. Lazzeri, C. Casiraghi, K.S. Novoselov, A.K. Geim, A.C. Ferrari, F. Mauri, Breakdown of the adiabatic Born-Oppenheimer approximation in graphene. Nat. Mater. **6**, 198–201 (2007)
44. J.E. Lee, G. Ahn, J. Shim, Y.S. Lee, S. Ryu, Optical separation of mechanical strain from charge doping in graphene. Nat. Commun. **3**, 1024 (2012)
45. M. Bruna, A.K. Ott, M. Ijas, D. Yoon, U. Sassi, A.C. Ferrari, Doping dependence of the Raman spectrum of defected graphene. ACS Nano **8**, 7432–7441 (2014)
46. Y.F. Hao, Y.Y. Wang, L. Wang, Z.H. Ni, Z.Q. Wang, R. Wang, C.K. Koo, Z.X. Shen, J.T.L. Thong, Probing layer number and stacking order of few-layer graphene by Raman spectroscopy. Small **6**, 195–200 (2010)
47. K.F. Mak, L. Ju, F. Wang, T.F. Heinz, Optical spectroscopy of graphene: from the far infrared to the ultraviolet. Solid State Commun. **152**, 1341–1349 (2012)
48. C.W. Luo, P.S. Tseng, H.J. Chen, K.H. Wu, L.J. Li, Dirac fermion relaxation and energy loss rate near the Fermi surface in monolayer and multilayer graphene. Nanoscale **6**, 8575–8578 (2014)
49. E. del Corro, L. Kavan, M. Kalbac, O. Frank, Strain assessment in graphene through the Raman 2D' mode. J. Phys. Chem. C **119**, 25651–25656 (2015)
50. N. Ferralis, Probing mechanical properties of graphene with Raman spectroscopy. J. Mater. Sci. **45**, 5135–5149 (2010)
51. T.M.G. Mohiuddin, A. Lombardo, R.R. Nair, A. Bonetti, G. Savini, R. Jalil, N. Bonini, D.M. Basko, C. Galiotis, N. Marzari, K.S. Novoselov, A.K. Geim, A.C. Ferrari, Uniaxial strain in graphene by Raman spectroscopy: G peak splitting, Gruneisen parameters, and sample orientation. Phys. Rev. B. **79** (2009)
52. C.W. Wang, M.D. Frogley, G. Cinque, L.Q. Liu, A.H. Barber, Molecular force transfer mechanisms in graphene oxide paper evaluated using atomic force microscopy and in situ synchrotron micro FT-IR spectroscopy. Nanoscale **6**, 14404–14411 (2014)
53. B. Partoens, F.M. Peeters, From graphene to graphite: electronic structure around the K point. Phys. Rev. B **74**, 075404 (2006)
54. J.R. Kyle, A. Guvenc, W. Wang, M. Ghazinejad, J. Lin, S. Guo, C.S. Ozkan, M. Ozkan, Centimeter-scale high-resolution metrology of entire CVD-grown graphene sheets. Small **7**, 2599–2606 (2011)
55. W. Li, S. Moon, M. Wojcik, K. Xu, Direct optical visualization of graphene and its nanoscale defects on transparent substrates. Nano Lett. **16**, 5027–5031 (2016)

56. A.C. Ferrari, Raman spectroscopy of graphene and graphite: disorder, electron-phonon coupling, doping and nonadiabatic effects. Solid State Commun. **143**, 47–57 (2007)
57. R. Rao, R. Podila, R. Tsuchikawa, J. Katoch, D. Tishler, A.M. Rao, M. Ishigami, Effects of layer stacking on the combination Raman modes in graphene. ACS Nano **5**, 1594–1599 (2011)
58. C. Cong, T. Yu, R. Saito, G.F. Dresselhaus, M.S. Dresselhaus, Second-order overtone and combination Raman modes of graphene layers in the range of 1690−2150 cm−1. ACS Nano **5**, 1600–1605 (2011)
59. J. dos Santos, N.M.R. Peres, A.H. Castro, Graphene bilayer with a twist: electronic structure. Phys. Rev. Lett. **99**, 4 (2007)
60. K. Kim, S. Coh, L.Z. Tan, W. Regan, J.M. Yuk, E. Chatterjee, M. Crommie, M.L. Cohen, S.G. Louie, A. Zettl, Raman spectroscopy study of rotated double-layer graphene: misorientation-angle dependence of electronic structure. Phys. Rev. Lett. **108**, 246103 (2012)
61. V. Carozo, C.M. Almeida, E.H. Ferreira, L.G. Cançado, C.A. Achete, A. Jorio, Raman signature of graphene superlattices. Nano Lett. **11**, 4527–4534 (2011)
62. R.W. Havener, H. Zhuang, L. Brown, R.G. Hennig, J. Park, Angle-resolved Raman imaging of interlayer rotations and interactions in twisted bilayer graphene. Nano Lett. **12**, 3162–3167 (2012)
63. J.-B. Wu, X. Zhang, M. Ijäs, W.-P. Han, X.-F. Qiao, X.-L. Li, D.-S. Jiang, A.C. Ferrari, P.-H. Tan, Resonant Raman spectroscopy of twisted multilayer graphene. Nat. Commun. **5**, 5309 (2014)
64. C.J. Tabert, E.J. Nicol, Optical conductivity of twisted bilayer graphene. Phys. Rev. B **87**, 121402 (2013)
65. A.A. Avetisyan, B. Partoens, F.M. Peeters, Stacking order dependent electric field tuning of the band gap in graphene multilayers. Phys. Rev. B **81**, 115432 (2010)
66. C.H. Lui, Z. Li, Z. Chen, P.V. Klimov, L.E. Brus, T.F. Heinz, Imaging stacking order in few-layer graphene. Nano Lett. **11**, 164–169 (2011)
67. C. Cong, T. Yu, K. Sato, J. Shang, R. Saito, G.F. Dresselhaus, M.S. Dresselhaus, Raman characterization of ABA-and ABC-stacked trilayer graphene. ACS Nano **5**, 8760–8768 (2011)
68. K.F. Mak, J. Shan, T.F. Heinz, Electronic structure of few-layer graphene: experimental demonstration of strong dependence on stacking sequence. Phys. Rev. Lett. **104**, 176404 (2010)
69. M.M. Lucchese, F. Stavale, E.H.M. Ferreira, C. Vilani, M.V.O. Moutinho, R.B. Capaz, C.A. Achete, A. Jorio, Quantifying ion-induced defects and Raman relaxation length in graphene. Carbon **48**, 1592–1597 (2010)
70. L.G. Cancado, A. Jorio, E.H.M. Ferreira, F. Stavale, C.A. Achete, R.B. Capaz, M.V.O. Moutinho, A. Lombardo, T.S. Kulmala, A.C. Ferrari, Quantifying defects in graphene via Raman spectroscopy at different excitation energies. Nano Lett. **11**, 3190–3196 (2011)
71. A. Eckmann, A. Felten, A. Mishchenko, L. Britnell, R. Krupke, K.S. Novoselov, C. Casiraghi, Probing the nature of defects in graphene by Raman spectroscopy. Nano Lett. **12**, 3925–3930 (2012)
72. R. Beams, L.G. Cancado, L. Novotny, Raman characterization of defects and dopants in graphene. J. Phys.Condens. Matter **27**, 083002 (2015)
73. A.A.K. King, B.R. Davies, N. Noorbehesht, P. Newman, T.L. Church, A.T. Harris, J.M. Razal, A.I. Minett, A new Raman metric for the characterisation of graphene oxide and its derivatives. Sci. Report. **6**, 19491 (2016)
74. B. Li, T. He, Z. Wang, Z. Cheng, Y. Liu, T. Chen, W. Lai, X. Wang, X. Liu, Chemical reactivity of C-F bonds attached to graphene with diamines depending on their nature and location. Phys. Chem. Chem. Phys. **18**, 17495–17505 (2016)
75. Z. Gan, H. Xu, Y. Hao, Mechanism for excitation-dependent photoluminescence from graphene quantum dots and other graphene oxide derivates: consensus, debates and challenges. Nanoscale **8**, 7794–7807 (2016)
76. G. Eda, Y.Y. Lin, C. Mattevi, H. Yamaguchi, H.A. Chen, I.S. Chen, C.W. Chen, M. Chhowalla, Blue photoluminescence from chemically derived graphene oxide. Adv. Mater. **22**, 505–509 (2010)

77. L. Cao, M.J. Meziani, S. Sahu, Y.P. Sun, Photoluminescence properties of graphene versus other carbon nanomaterials. Acc. Chem. Res. **46**, 171–180 (2013)
78. S.K. Pal, Versatile photoluminescence from graphene and its derivatives. Carbon **88**, 86–112 (2015)
79. C. Galande, A.D. Mohite, A.V. Naumov, W. Gao, L.J. Ci, A. Ajayan, H. Gao, A. Srivastava, R.B. Weisman, P.M. Ajayan, Quasi-molecular fluorescence from graphene oxide. Sci. Report. **1** (2011)
80. C.T. Chien, S.S. Li, W.J. Lai, Y.C. Yeh, H.A. Chen, I.S. Chen, L.C. Chen, K.H. Chen, T. Nemoto, S. Isoda, M.W. Chen, T. Fujita, G. Eda, H. Yamaguchi, M. Chhowalla, C.W. Chen, Tunable photoluminescence from graphene oxide. Angew. Chem.Int. Ed. **51**, 6662–6666 (2012)
81. M.S. Dresselhaus, A. Jorio, M. Hofmann, G. Dresselhaus, R. Saito, Perspectives on carbon nanotubes and graphene Raman spectroscopy. Nano Lett. **10**, 751–758 (2010)
82. J. Maultzsch, H. Telg, S. Reich, C. Thomsen, Radial breathing mode of single-walled carbon nanotubes: optical transition energies and chiral-index assignment. Phys. Rev. B **72**, 205438 (2005)
83. S. Kim, D. Hee Shin, C.O. Kim, S. Seok Kang, S. Sin Joo, S.-H. Choi, S. Won Hwang, C. Sone, Size-dependence of Raman scattering from graphene quantum dots: interplay between shape and thickness. Appl. Phys. Lett. **102**, 053108 (2013)
84. S. Ryu, J. Maultzsch, M.Y. Han, P. Kim, L.E. Brus, Raman spectroscopy of lithographically patterned graphene nanoribbons. ACS Nano **5**, 4123–4130 (2011)
85. Z.Q. Luo, T. Yu, Z.H. Ni, S.H. Lim, H.L. Hu, J.Z. Shang, L. Liu, Z.X. Shen, J.Y. Lin, Electronic structures and structural evolution of hydrogenated graphene probed by Raman spectroscopy. J. Phys. Chem. C **115**, 1422–1427 (2011)
86. I.A. Verzhbitskiy, M. De Corato, A. Ruini, E. Molinari, A. Narita, Y. Hu, M.G. Schwab, M. Bruna, D. Yoon, S. Milana, X. Feng, K. Mullen, A.C. Ferrari, C. Casiraghi, D. Prezzi, Raman fingerprints of atomically precise graphene nanoribbons. Nano Lett. **16**, 3442–3447 (2016)
87. J.Z. Shang, L. Ma, J.W. Li, W. Ai, T. Yu, G.G. Gurzadyan, The origin of fluorescence from graphene oxide. Sci. Report. **2**, 792 (2012)
88. J.A. Yan, M.Y. Chou, Oxidation functional groups on graphene: structural and electronic properties. Phys. Rev. B. **82** (2010)
89. K.F. Mak, C.H. Lui, J. Shan, T.F. Heinz, Observation of an electric-field-induced band gap in bilayer graphene by infrared spectroscopy. Phys. Rev. Lett. **102**, 256405 (2009)
90. R.R. Hartmann, J. Kono, M.E. Portnoi, Terahertz science and technology of carbon nanomaterials. Nanotechnology **25**, 322001 (2014)
91. D. Sun, C. Divin, C. Berger, W.A. de Heer, P.N. First, T.B. Norris, Spectroscopic measurement of interlayer screening in multilayer epitaxial graphene. Phys. Rev. Lett. **104**, 136802 (2010)
92. G.X. Wang, B. Wang, J. Park, Y. Wang, B. Sun, J. Yao, Highly efficient and large-scale synthesis of graphene by electrolytic exfoliation. Carbon **47**, 3242–3246 (2009)
93. D.R. Lenski, M.S. Fuhrer, Raman and optical characterization of multilayer turbostratic graphene grown via chemical vapor deposition. J. Appl. Phys. **110**, 013720–013720-4 (2011)
94. R.W. Havener, C.J. Kim, L. Brown, J.W. Kevek, J.D. Sleppy, P.L. McEuen, J. Park, Hyperspectral imaging of structure and composition in atomically thin heterostructures. Nano Lett. **13**, 3942–3946 (2013)
95. M. Hofmann, Y.P. Hsieh, K.W. Chang, H.G. Tsai, T.T. Chen, Dopant morphology as the factor limiting graphene conductivity. Sci. Report. **5** , 17393 (2015)
96. A. Bosca, J. Pedros, J. Martinez, T. Palacios, F. Calle, Automatic graphene transfer system for improved material quality and efficiency. Sci. Report. **6**, 21676 (2016)
97. N.E. Leadbeater, R.J. Smith, Real-time monitoring of microwave-promoted Suzuki coupling reactions using in situ Raman spectroscopy. Org. Lett. **8**, 4588–4591 (2006)
98. J.R. Schmink, J.L. Holcomb, N.E. Leadbeater, Use of Raman spectroscopy as an in situ tool to obtain kinetic data for organic transformations. Chem. Eur. J. **14**, 9943–9950 (2008)